Materials Science and Engineering C 37 (2014) 195–203

Contents lists available at ScienceDirect

Materials Science and Engineering C

journal homepage: www.elsevier.com/locate/msec

Synthesis and characterization of xanthan–hydroxyapatite nanocomposites for cellular uptake

Vania Blasques Bueno [a], Ricardo Bentini [a], Luiz Henrique Catalani [a], Leandro R.S. Barbosa [b], Denise Freitas Siqueira Petri [a,*]

[a] Instituto de Química, Universidade de São Paulo, P.O. Box 26077, São Paulo, SP 05513-970, Brazil
[b] Instituto de Física, DFGE, Universidade de São Paulo, São Paulo, 05508-090 SP, Brazil

ARTICLE INFO

Article history:
Received 13 September 2013
Received in revised form 8 December 2013
Accepted 5 January 2014
Available online 10 January 2014

Keywords:
Hydroxyapatite
Xanthan
Nanocomposite hydrogels
Osteoblast growth

ABSTRACT

In this work xanthan–nanohydroxyapatite (XnHAp) and its equivalent strontium substituted (XnHApSr) were synthesized by the precipitation of nanohydroxyapatite in xanthan aqueous solution, characterized and compared to conventional hydroxyapatite particles (HAp). XnHAp and XnHApSr were less crystalline than HAp, as revealed by X-ray diffraction. Xanthan chains enriched the surface of XnHAp and XnHApSr particles, increasing the zeta potential values from $-(7 \pm 1)$ mV, determined for HAp, to $-(17 \pm 3)$ mV and $-(25 \pm 3)$ mV, respectively. This effect led to high colloidal stability of XnHAp and XnHApSr dispersions and acicular particles (140 ± 10) nm long and (8 ± 2) nm wide, as determined by scanning electron microscopy and atomic force microscopy. XnHAp and XnHApSr particles were added to xanthan hydrogels to produce compatible nanocomposites (XCA/XnHAp and XCA/XnHApSr). Dried nanocomposites presented surface energy, Young's modulus and stress at break values comparable to those determined for bare xanthan matrix. Moreover, adding XnHAp or XnHApSr nanoparticles to xanthan hydrogel did not influence its porous morphology, gel content and swelling ratio. XCA/XnHAp and XCA/XnHApSr composites proved to be suitable for osteoblast growth and particularly XCA/XnHapSr composites induced higher alkaline phosphatase activity.

1. Introduction

Hydrogels are of great interest as scaffolds for cell culture, due to their similarity to extracellular matrix [1,2]. Particularly polysaccharide hydrogels are advantageous for biomedical applications, because they join biocompatibility, biodegradability, and abundance in nature with hydrogels similar to biological systems [3]. Some examples include the use of chitosan, alginates, and celluloses for drug delivery, protein immobilization, wound dressings, cell encapsulation and tissue engineering [4–10].

Hydroxyapatites (HAp) are the major inorganic component in skeletal tissue (about 50 wt.% of hard tissues is composed of calcium and phosphate ions) [11]. For this reason, there is an increasing interest on calcium phosphates in biological applications, which include bone cavity filling, osteologic implants and drug delivery, due to its bioactivity, biocompatibility and mechanical properties [12]. On the other hand, the benefits of strontium compounds, as for instance, strontium ranelate, against osteoporosis made them a well recommended therapy [13]. For this reason, HAp has been modified with strontium to enhance its biological activity. The replacement of calcium by strontium in the HAp structure has proven to be an efficient strategy for improving bone formation due to better osteoblast spreading and proliferation [14]. In comparison to poly(methyl methacrylate) bone cement, bioactive bone cements based on Sr-HAp present better adhesion, biocompatibility, bioactivity and osteoconductivity [15,16]. These issues motivate the search for new scaffolds for bone regeneration based on Sr-HAp.

Nevertheless, pure HAp is brittle and the devices prepared from this material can present poor mechanical performance [17,18]. To overcome these drawbacks, HAp composites or nanocomposites have been used; for instance, composites of collagen and HAp, in a 1:1 volumetric ratio have been successfully applied [19].

Hydroxyapatite and nanohydroxyapatites (nHAp) [12] can be combined with a large number of natural and synthetic polymers [20]. However, the lack of adhesion between the inorganic and the polymeric phase will result in failure at the interface causing deterioration of the mechanical properties [21]. Alternatives to enhance nHAp compatibilization and avoid nanoparticle agglomeration include its surface functionalization, for example with PLLA, alginate, chitosan and silanes [20,22–24], or *in situ* synthesis of nHAp in polymeric solutions [25,26]. Besides nHAp functionalization allows strong bond formation between nHAp and polymer matrices as an intermediate layer, their modified surface acts in modulating their colloid stability and in preventing dissolution in low pH and inflammatory response [27,28].

Nanocomposite hydrogels are soft materials consisting of a unique organic/inorganic network structure, with interesting characteristics, as mechanical, optical, and swelling/de-swelling properties [29–31].

* Corresponding author. Tel.: +55 11 30913831; fax: +55 11 3815 5579.
E-mail addresses: dfsp@usp.br, dfsp@iq.usp.br (D.F.S. Petri).

0928-4931/$ – see front matter © 2014 Elsevier B.V. All rights reserved.
http://dx.doi.org/10.1016/j.msec.2014.01.002

Compatibilization between nanohydroxyapatite and hydrogels is important for adequate and homogeneous hydroxyapatite distribution in hydrogel matrix, to obtain nanocomposite hydrogels. These materials have many applications on biomedical science, as drug delivery systems, scaffolds for cellular culture and bone cavity filling [32–34].

Xanthan gum is a high molecular weight polysaccharide with branched chains and acidic characteristics, produced by *Xanthomonas campestris* [35]. Their derivatives are used as thickener agent in food, cosmetics and drilling fluids [35,36]. Moreover, intra-articular injection of xanthan gum could protect joint cartilage and reduce osteoarthritis progression, being an effective therapeutic method of this disease [37]. O-acetyl and pyruvyl residues present at its structure are deprotonated at pH ≥ 4.5, enabling their physical crosslinking mediated by Ca^{2+} ions, to form physical hydrogels [38,39]. Xanthan can also be crosslinked by using citric acid as crosslinking agent to form xanthan-citric acid (XCA) chemical hydrogels [40], which carry and deliver proteins as bovine serum albumin and lysozyme [41]. Recently we have described a fast and simple method to prepare composite films of magnetite nanoparticles and XCA networks with coercivity of 27 ± 2 Oe at 300 K), which were successful on the development of scaffolds for the proliferation of fibroblast, particularly when an external magnetic field was applied [42].

This work describes the creation of compatible XCA/hydroxyapatite hydrogel nanocomposites, by using xanthan modified nanohydroxyapatite (XnHAp) and its equivalent strontium substituted (XnHApSr). The nanoparticles were obtained by precipitation in xanthan solution. Nanoparticle stability and the particles homogeneity distribution on hydrogel matrices were evaluated. The nanocomposite hydrogels made of xanthan modified hydroxyapatites and XCA were tested as scaffolds for osteoblast growth.

2. Experimental

2.1. Materials

Commercial xanthan (Kelzan®, CP Kelco, USA, degree of pyruvate = 0.38, degree of acetyl = 0.41, M_v ~ 1.0 10^6 g/mol, degree of polymerization ~ 1072) was used as received. Citric acid (Analitica Quimica, Brazil) was recrystallized twice from water prior to use. $Ca(OH)_2$, $Sr(CH_3COO)_2$ and H_3PO_4 were obtained from Givaudan, Sigma-Aldrich and Synth (Brazil) respectively. Deionized water was used in all experiments.

2.2. Methods

2.2.1. Nanoparticle synthesis

Xanthan-hydroxyapatite particles (XnHAp) were obtained as follows: 0.93 g of $Ca(OH)_2$ (0.013 mol) were added to 0.5 L of xanthan solution at 1 g L^{-1} at (50 ± 1) °C under vigorous stirring (Ika Turrax®, 18,000 rpm). After total homogenization 0.2 mol L^{-1} H_3PO_4 solution was added dropwise until medium achieved pH ~7.5, as schematically represented in the Supplementary Material Figure S1A. The resultant dispersion was dialyzed against deionized water until the conductivity of dialysis water reached 5 μS/cm. nHAp particles were obtained by the same procedure, but in the absence of xanthan. Xanthan-strontium-substituted hydroxyapatite particles (XnHApSr) were obtained as follows: 0.836 g of $Ca(OH)_2$ (0.011 mol) and 0.093 g of $Sr(CH_3COO)_2$ (0.0004 mol) were added to 0.5 L of xanthan solution at 1 g L^{-1} at (50 ± 1) °C under vigorous stirring (Ika Turrax®, 18,000 rpm). After total homogenization 0.2 mol L^{-1} H_3PO_4 solution was added dropwise until medium achieved pH ~7.5, as schematically represented in the Supplementary Material Figure S1B. The resultant dispersion was dialyzed against deionized water until the conductivity of dialysis water reached 5 μS/cm. nHAp particles were obtained by the same procedure, but in the absence of xanthan. Dispersions were freeze-dried to obtain nHAp, XnHAp and XnHApSr nanoparticle powders.

2.2.2. Nanoparticle characterization

Nanoparticle characterization was done by means of inductively coupled plasma atomic emission spectroscopy (ICP-AES), X-ray diffraction, thermogravimetric analysis (TGA), Fourier-transform infrared spectroscopy (FTIR), scanning electron microscopy (SEM), atomic force microscopy (AFM), dynamic light scattering (DLS) and zeta potential. ICP-AES was performed in a Spectro Cirus CCD apparatus. X-ray diffraction analyses were performed with a Rigaku Miniflex diffractometer (Cu, Kα; λ = 1.5418 Å, ~8 keV), with a goniometer θ:2θ based on Bragg–Brentano geometry. X-ray Scattering slit and receiving slit were 4.2° and 0.3 mm, respectively. Divergence slit was variable. Scan mode was continuous, scan speed was 0.100°/min and sampling width was 0.010°. Diffractograms were analyzed with Crystallographica Search-Match software. FTIR was performed with BOMEM MB 100 equipment using KBr pellets. SEM analysis was performed in a Jeol microscope FEG7401F equipped with a Field-Emission Gun, after coating the samples with a thin gold layer. Sizes obtained from SEM images were calculated using AxioVision V. 4.6.3.0 program, by measuring randomly >100 particles. For atomic force microscopy (AFM), diluted particles suspension was dropped onto Si/SiO_2 wafers and dried at 25 °C for 24 h. AFM was performed in air using a PicoSPM-LE Molecular Imaging system with cantilevers operating in the intermittent contact mode (AAC mode). DLS and zeta potential (ζ-potential) measurements were performed in a commercial instrument Zetasizer NanoZS (Malvern, UK). A He–Ne laser was used as a light source with wavelength λ = 633 nm. Concerning the DLS experiments, the intensity of light scattered was recorded at an angle of 90° with an avalanche photodiode detector. We used the Zetasizer Software 6.2 (provided by Malvern) to determine the particle size distribution, using the correlation function to obtain the distributions of the decay rates, and the apparent diffusion coefficients. Finally, the distributions of the hydrodynamic radius of the scattering particles in solution are estimated *via* Stokes–Einstein equation. DLS and ζ-potential measurements were performed for dispersions of nHAp, XnHAp and XnHApSr at 1 g L^{-1} after filtering through a 0.45 μm Millipore filter. Droplets of the filtered dispersions were deposited onto Si wafers and allowed to dry slowly at room temperature for AFM analyses in air, using a PicoSPM-LE Molecular Imaging system with cantilevers operating in the intermittent contact mode (AAC mode).

Colloidal stability of nHAp, XnHAp and XnHApSr nanoparticles dispersed in distilled water (pH ~ 6) at 1.0 g/L was monitored using a LUMiReader®414 Separation Analyzer (L.U.M. GmbH, Germany), by the SEP View 4.01 software, which registered the normalized integral light transmission as a function of time at (26 ± 2) °C. Glass cuvettes (10 mm diameter and 80 mm length) were used for the experiments. At the beginning, the dispersion is homogeneous and the transmitted light through the cuvette is very low. As time goes by, the dispersion starts to destabilize, mainly because the density of hydroxyapatite is 2.95 g/cm^3 [43], which is larger than the water density. For this reason, particles sediment, accumulating at the bottom of the cuvette and increasing the transmission of light through the upper liquid. Measurements were done in triplicate. The intensity of light transmitted through pure water was used as reference for 100% light transmittance.

2.2.3. Production and characterization of nanocomposite hydrogels

Xanthan based nanocomposite hydrogels were prepared as schematically represented in the Supplementary Material Figure S2A and S2B, by casting a 6 g L^{-1} xanthan aqueous solution containing nanoparticles (nHAp, XnHAp or XnHApSr) at 0.6 g L^{-1} (10% filler content) or 1.8 g L^{-1} (30% filler content) in the presence of citric acid at 0.3 g L^{-1}. Previously the dispersions were homogenized with an Ika Turrax® stirrer at 18,000 rpm for 3 minutes and submitted to centrifugation for 5 min at 3600 rpm to remove air bubbles. Crosslinking was achieved

by heating the films at 165 °C for 7 min, as described elsewhere [40,41]. The resulting xanthan hydrogels were swollen in water for 24 h and freeze-dried.

Gel content and swelling degree at equilibrium (Q) were calculated according to Eqs. (1) and (2), respectively:

$$\text{Gel content}(\%) = \left[1-\left(\frac{m_{pol}-m_{driedgel}}{m_{pol}}\right)\right]x100 \quad (1)$$

$$Q = \frac{m_{water}}{m_{driedgel}} = \frac{m_{swollengel}-m_{driedgel}}{m_{driedgel}} \quad (2)$$

where m_{pol} is the initial mass of polymer, $m_{driedgel}$ is the mass of dried hydrogel, m_{water} is the amount of water absorbed by the gel and $m_{swollengel}$ is the mass of swollen hydrogel.

The morphology of cryofractured surfaces of freeze-dried nanocomposite hydrogels was analyzed by SEM. Dried nanocomposites were characterized by means of FTIR using KBr pellets. Mechanical properties of dried nanocomposite films (~0.010 mm thick, and rectangular dimensions of ~30 mm × ~6 mm) were investigated in a DMA Q800 from TA Instruments.

For atomic force microscopy (AFM) and contact angle measurements nanocomposite thin films were obtained by the adsorption of xanthan/nanohydroxyapatites dispersion onto Si/SiO_2 wafers in the presence of citric acid (same conditions used for the nanocomposite hydrogel preparation) and $CaCl_2$ 1.0 mmol L^{-1} at pH 10.0 during 24 h, at 25 °C. $CaCl_2$ was added because Ca^{2+} ions mediate the binding between xanthan carboxylate groups and surface silanol groups [44]. After drying samples were crosslinked at 165 °C under the same conditions of the films obtained by casting. AFM was performed in air using a PicoSPM-LE Molecular Imaging system with cantilevers operating in the intermittent contact mode (AAC mode). The contact angles were determined by the sessile-drop method at (24 ± 1) °C in a home-built apparatus [45]. Sessile solvent drops of 4 μL were gentle deposited on the thin film and stabilized for 20 s before taking images. The surface energy (γ^S) of the films was assessed by means of contact angles (θ) performed with drops (8 μL) of diiodomethane ($\gamma^L = 50.8$ mJ m^2; $\gamma^p{}_L = 2.3$ mJ m^2 and $\gamma^d{}_L = 48.5$ mJ m^2) and formamide ($\gamma^L = 58.2$ mJ m^2; $\gamma^p{}_L = 18.7$ mJ m^2 and $\gamma^d{}_L = 39.5$ mJ m^2) [46]. Water was not used because hydrogel thin film swelling affects the drop format. The polar (γ^p) and dispersive (γ^d) components of the surface energy were determined by Owens–Wendt's equation [47], also known as geometric mean equation. At least three films of the same sample were analyzed.

2.2.4. Cell adhesion and proliferation assays

Nanocomposite hydrogels samples were cut in circular scaffolds (diameter 12 mm) and exposed to UV light during 15 min each side for sterilization. These samples were placed in cell culture clusters (Costar, Corning, NY, USA) and soaked in DMEM medium supplemented with 10% of fetal bovine serum (FBS) containing penicillin (100 IU mL^{-1}), streptomycin (100 mg L^{-1}) and amphotericin B (50 g L^{-1}) for 24 h before cell seeding. The medium was removed and OFCOLL II osteoblasts were seeded at a density of 4.4×10^4 cells cm^{-2} in 25 μL of supplemented DMEM. After 2 h of incubation, 250 μL of culture medium (supplemented DMEM) was added. The complete media was refreshed every 2 days. The samples were incubated at 37 °C and 5% CO_2 atmosphere. For proliferation assay, scaffolds were rinsed once with PBS solution and placed in a new well plate containing 300 μL of DMEM with MTT (0.5 g L^{-1}) in every well. After 3 h, solution was removed and 1 mL of DMSO was added to each well to dissolve MTT-formazan crystals. Aliquots (500 μL) were taken in order to measure the absorbance at 570 nm (Shimadzu Multispec-1501).

2.2.5. Alkaline phosphatase (ALP) assay

OFCOLL II osteoblast culture cells on scaffolds at day 21 were lysed using a lysis buffer containing 1% Triton X-100, 0.9% NaCl and 0.5 M Tris pH 9.0. The lysates were centrifuged at 12,000 rpm for 15 min at 4 °C and supernatants were collected. ALP assay activity was performed according to manufacturer's instructions, using a colorimetric ALP assay kit (Labtest, Montes Claros, Minas Gerais, Brazil). Briefly, 50 μL of supernatant was incubated with substrate for 10 min and the reaction was stopped with a colorimetric reagent (thymolphthalein) before reading absorbance at 590 nm in a Shimadzu spectrophotometer MultiSpec-1501 nm. ALP activity calculations were normalized by cell number, obtained by MTT test. ALP is related to one of the functional genes expressed in the process of calcification and its increase reflects mineralization process of the neotissue [48].

2.2.6. Statistical analyses

Cell proliferation and ALP activity data values were expressed as mean values with the corresponding standard deviations (n = 3). One way analysis of variance (ANOVA) with post hoc test was used to evaluate the differences of variables among groups. A value of $p < 0.05$ was considered a significant difference. Analyses were carried out in Excel 2013® for Windows® (Microsoft Office Home and Student®, 2013).

3. Results and discussion

3.1. Production and characterization of xanthan-modified hydroxyapatite nanoparticles

The production of XnHAp and XnHApSr particles is schematically depicted in the Supplementary Material, Figure S1A. Initially Ca^{2+} ions are dissolved at pH 10 in the presence of xanthan chains. Calcium ions are chelated by xanthan chains, forming nucleation sites for hydroxyapatite crystal growth. As phosphoric acid is added to the solutions, the medium pH decreases to ~7.5, promoting the precipitation of Ca^{2+} ions as hydroxyapatite (nHAp):

$$10\ Ca(OH)_2 + 6\ H_3PO_4 \rightarrow Ca_{10}(PO_4)_6(OH)_2 + 18\ H_2O \quad (3)$$

FTIR spectra (Supplementary Material, Figure S3A) obtained for all synthesized hydroxyapatite nanoparticles presented typical bands of PO_4^{3-} vibrations: bending at 1033 cm^{-1}, 603.67 cm^{-1} and 565.10 cm^{-1} [49]. The band at ~1640 cm^{-1} and the broad band ~3500 cm^{-1} were attributed to OH bending and stretching modes [50]. The band intensity at ~1640 cm^{-1} was more intense in the spectra obtained for XnHAp than in nHAp, because the xanthan carbonyl groups in the former absorb in the same spectral region as OH groups. The spectra obtained for pure xanthan indicated an absorption band 1728 cm^{-1}, which was attributed to the carbonyl stretching of carboxylic acid groups. This band does not appear in XnHAp spectra, due to alkaline conditions, which promote the carboxylic acid dissociation. Such xanthan dissociated carboxylate groups act as binding sites to calcium ions [38,39]. Similar behavior was observed in hydroxyapatite synthesized in chitosan/pectin polyelectrolyte complex solutions [25], where pectin carboxylate groups interacted with calcium ions.

X-ray diffraction patterns obtained for pure hydroxyapatite (nHAp), XnHAp and XnHApSr in Fig. 1 presented the main characteristic hydroxyapatite diffraction peaks, indicated by blue crosses in Fig. 1 [51]. Diffractograms obtained for XnHAp and XnHApSr presented peak broadening in comparison to HAp (See supplementary material, Figure S4), evidencing a smaller degree of crystallinity of XnHAp and XnHApSr in comparison to nHAp [52]. The crystallinity decrease was more pronounced for XnHAp than for XnHAPS. ICP-AES results (Supplementary Material, Figure S3B) revealed that XnHAp and XnHApSr samples presented Ca/P molar ratio of 2.2 and 2.6, respectively. Ca/P molar ratio reported in the literature for biological apatites ranges

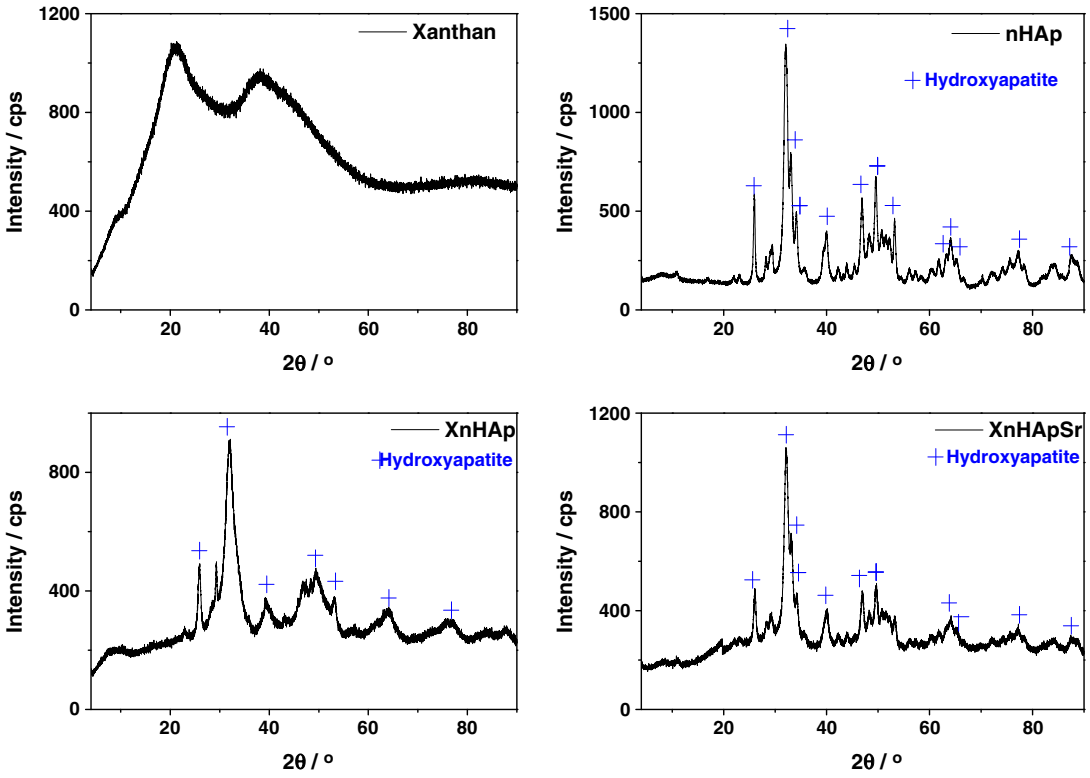

Fig. 1. XRD patterns obtained for pure xanthan, nHAp, XnHAp and XnHApSr along with the characteristic hydroxyapatite diffraction peaks, represented by the blue crosses. Details about peak fitting are shown in the Supplementary Material Figure S4.

from 1.5 to 1.85 [53]. The higher Ca/P ratio observed for synthesized XnHAp and XnHApSr samples can be related to the complexation of Ca^{2+} ions with xanthan carboxylate groups [38] combined with substitution of phosphate groups by carbonate, forming carbonated hydroxyapatite [53]. Strontium content in XnHApSr samples is about 1%, which corresponds to 7.7% of calcium amount.

SEM images in Fig. 2A, C and E indicated respectively that nHAp, XnHAp and XnHApSr nanoparticles are acicular particles with similar dimensions, with length of (140 ± 10) nm (See supplementary material, Figure S5) and width ranging from 5 to 10 nm (measured by AFM, see Supplementary Material, Figure S6), which corroborate with literature data [23,54]. The corresponding size distributions determined by DLS are presented in Fig. 2B, D and F. One should notice that the mean sizes determined by DLS refer to the particles dispersed in water and that the software considers all particles as spherical bodies; it cannot discriminate between ellipsoids and spheres. Therefore, the particles dimensions determined by DLS correspond to averaged sizes of length and width. The mean sizes of particles produced in the absence of xanthan (nHAp) amounted to (313 ± 45) nm, while those prepared in xanthan solution, namely XnHAp and XnHApSr, presented mean size of (56 ± 18) nm and (75 ± 18) nm, respectively. These figures indicate clearly that nHAp are aggregated in water and that particles preparation in the presence of xanthan chains avoids particles collapse. The ζ-potential values determined for nHAp, XnHAp and XnHApSr particles amounted to −(7 ± 1) mV, −(17 ± 3) mV and −(25 ± 3) mV. These findings show that during the precipitation reaction (Eq. (3)) xanthan chains carboxylate groups are on the particle surface, exposed to the medium, creating negative surface potential. Such negative surface potential avoids aggregation among the particles due to electrostatic repulsion and this effect explains the smaller sizes of XnHAp and XnHApSr in comparison to nHAp. This effect can be seen in AFM images (Supplementary material Figure S6), where nHAp appeared as frequent large clusters and some isolated particles ~7 nm high. In the case of XnHAp and XnHApSr samples, large clusters were not often observed and particles (5 nm to 10 nm high) appeared together with xanthan chains (Supplementary materials Figures S6B and S6C).

The colloidal stability of nHAp, XnHAp and XnHApSr dispersions at 3 g L^{-1} was analyzed at (26 ± 2) °C, determining the change of integral transmitted light as a function of time, as shown in Fig. 3. The data were normalized considering 100 % transmittance the transmitted light measured for the blank (water). As the time goes by, the nanocrystals sediment at the bottom of the cuvette, increasing the transmitted light. Therefore, the larger is the increase in transmittance as a function of time, the less stable is the colloidal dispersion. Fig. 3 shows important trends regarding the functionalization of the nHAp with xanthan. The transmittance for XnHAp and XnHApSr increased slowly and linearly with the time, indicating high stability, and after 4 h the transmittance increment was small (~14%), compared to bare nHAp (~72%). Thus, upon precipitating hydroxyapatite in the presence of xanthan, smaller and negatively charged particles with outstanding colloidal stability were produced.

3.2. Production and characterization of nanocomposite hydrogel films

The production of xanthan hydrogel nanocomposites with (A) XnHAp or (B) XnHApSr particles is schematically depicted in the Supplementary Material Figure S2. Recently the synthesis and characterization of xanthan and citric acid (XCA) hydrogels were reported [40,41]. Dehydration promoted crosslinking between citric acid and xanthan pyruvyl, acetyl and OH groups leading to hydrogels with high crosslinking density and charge density. Dried (Fig. 4A) and swollen (Fig. 4B) XCA hydrogels are homogeneous. However, dried (Fig. 4C) or swollen (Fig. 4D) XCA/nHAp composites are heterogeneous, evidencing that xanthan and nanohydroxyapatite are not compatible. On the other hand, XCA/XnHApSr and XCA/XnHAp nanocomposite films are apparently homogeneous (Fig. 4E to L). Therefore, the presence of xanthan chains on the surface of XnHAp and XnHApSr particles favored the compatibility between particles and xanthan matrix.

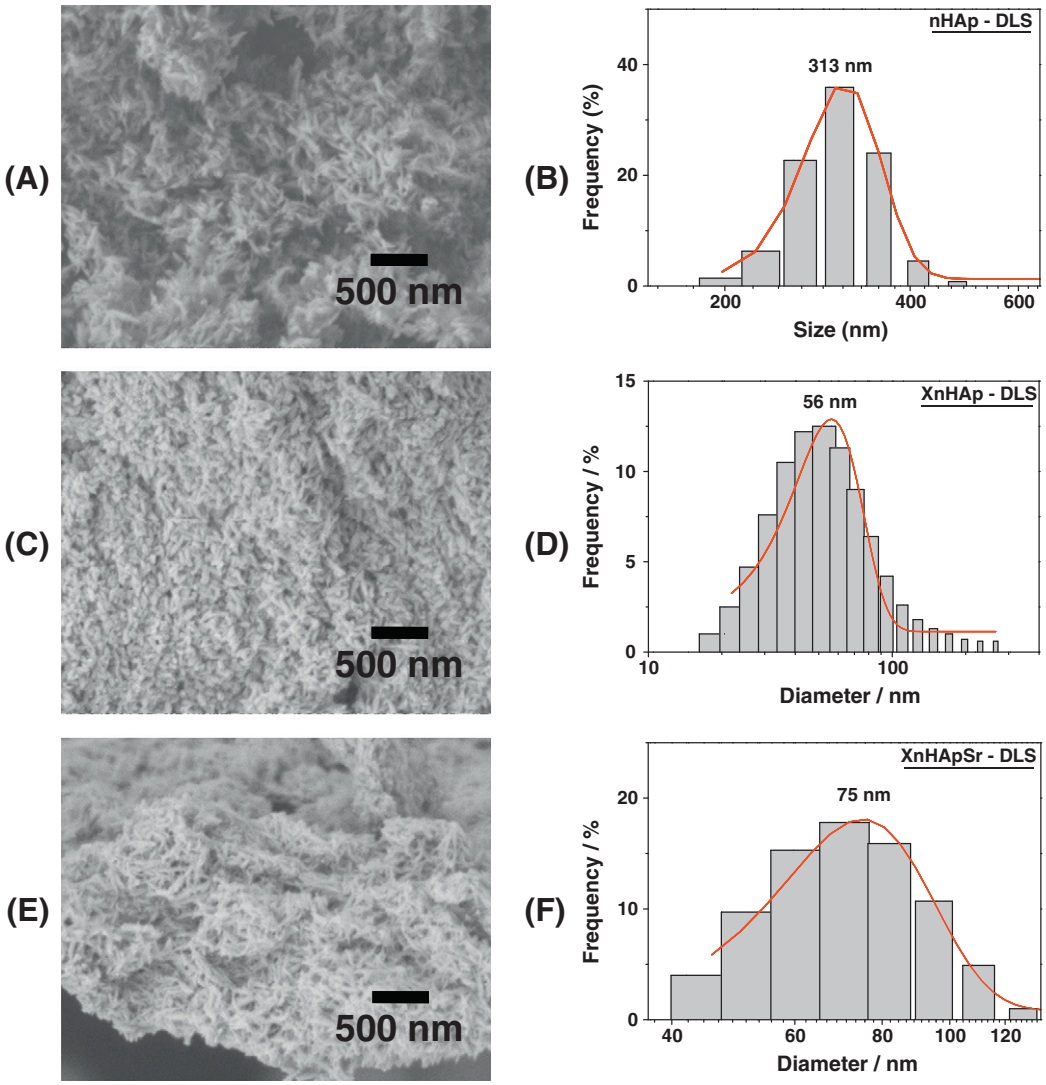

Fig. 2. SEM images and DLS particles size distribution for (A–B) nHAp, (C–D) XnHAp and (E–F) XnHApSr.

The Young's modulus (E) and stress at break (σ) values determined for bare XCA, XCA/HAp,XCA/XnHAp and XCA/XnHApSr hydrogels in dry state (collapsed) are shown in Fig. 5A and B, respectively. Despite the large standard deviation values, it is possible to observe that the addition of 10 wt.% XnHAp to XCA matrix led to more rigid materials, since the E values increased from (1.5 ± 0.4) GPa to (3.0 ± 0.7) GPa and σ values were similar. The addition of 10 wt.% XnHApSr particles to XCA matrix did not affect its mechanical properties, both E and σ values were similar. On the other hand, the addition of 10 wt.% HAp to XCA led to materials with poor mechanical properties; E values decreased from (1.5 ± 0.4) GPa to (0.2 ± 0.1) GPa and σ values decreased from (18 ± 4) MPa to (1.0 ± 0.5) MPa, because the adhesion between unmodified particles (nHAp) and matrix is very weak. Therefore these findings evidenced the compatibility between xanthan matrix and xanthan modified hydroxyapatite nanoparticles.

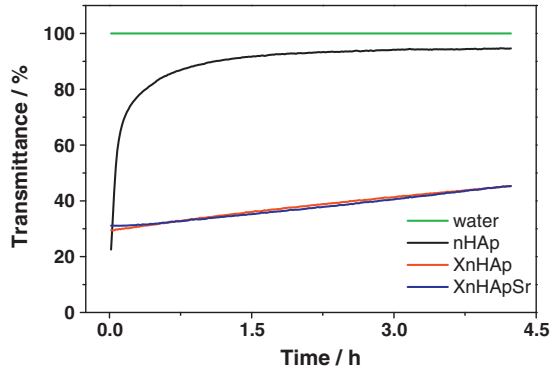

Fig. 3. Normalized integral light transmission determined as a function of time at (26 ± 2) °C for nHAp, XnHAp and XnHApSr nanoparticles dispersed in distilled water (pH ~ 6) at 1.0 g/L. Green line corresponds to 100% transmittance (water).

Although XCA/XnHApSr and XCA/XnHAp nanocomposite films 30 wt.% of filler are visually homogeneous (Fig. 4G, H, K and L), the mechanical properties of composites and bare XCA were comparable. No strong reinforcement effect could be observed probably due to heterogeneous dispersion of XnHAp or XnHApSr particles in the XCA matrix caused by drying process, which reduced the contact area [20]. The tensile strength values at break were similar for all samples (17 ± 3) MPa, except for XCA/nHAp, which was much smaller (1.0 ± 0.5) MPa (Fig. 5B), proving again that producing hydroxyapatite particles in the presence of xanthan is crucial for adequate adhesion between xanthan network and particles.

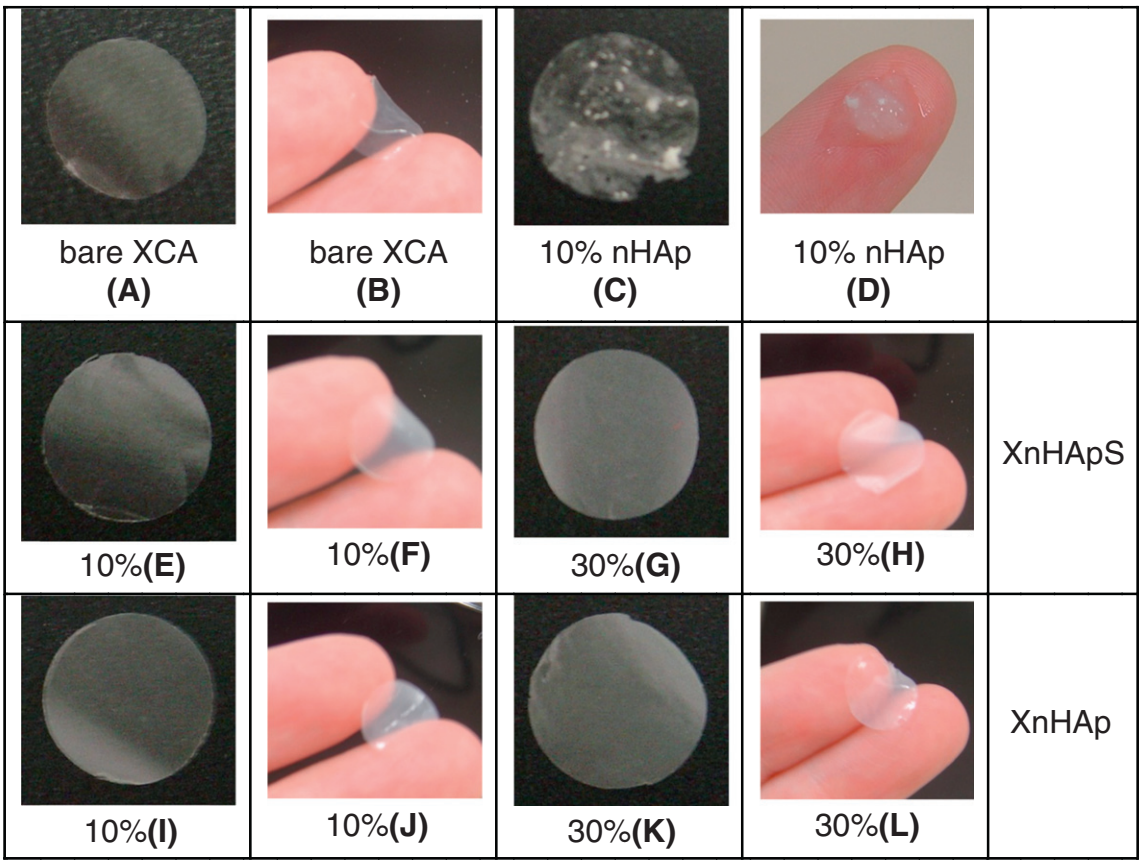

Fig. 4. Photographs taken for dried (A) and swollen (B) XCA hydrogels; dried (C) and swollen (D) XCA hydrogel nanocomposites with 10% nHAp; dried (E) and swollen (F) XCA hydrogel nanocomposites with 10% XnHApSr; dried (G) and swollen (H) XCA hydrogel nanocomposites with 30% XnHApSr; dried (I) and swollen (J) XCA hydrogel nanocomposites with 10% XnHAp; dried (K) and swollen (L) XCA hydrogel nanocomposites with 30% XnHAp.

The porous structure of freeze-dried bare XCA hydrogels, XCA/XnHAp 10 wt.% and XCA/XnHApSr 10 wt.% nanocomposite hydrogels presented in SEM images in Fig. 6A, B and C, respectively, was similar for all samples. However, the nanoparticles could not be visualized in the nanocomposites. AFM images of thin films of xanthan, XCA/XnHAp and XCA/XnHApSr nanocomposites adsorbed onto Si wafers are presented in Fig. 6D, E and F, respectively. In the absence of particles (Fig. 6D), the xanthan chains are densely packed and homogeneous distributed on the surface. In the presence of XnHAP (Fig. 6E) or XnHApSr (Fig. 6F) particles, xanthan fibrils and some nanoparticles distributed among them can be observed.

Gel content and swelling ratio (Q) determined for hydrogels containing or not xanthan modified hydroxyapatite particles were comparable (Table 1). Surface energy (γ^T) and the corresponding dispersive (γ^D) and polar (γ^P) components calculated from contact angles with droplets of formamide and CH_2I_2 on thin films of xanthan, XCA/XnHAp and XCA/XnHApSr nanocomposites adsorbed onto Si wafers are shown in Table 1 along with literature data for bare HAp [55]. Xanthan and HAp have similar surface energy values. That is the reason for the similar values found for nanocomposites.

3.3. Cell proliferations and ALP assays

Anselme and coworkers showed that the rate of cellular proliferation was linearly dependent on surface energy and increased with increasing hydrophobicity [56]. Fig. 7A shows that cellular proliferation was not influenced by the inclusion of functionalized nanohydroxyapatites in the hydrogels; no statistical difference was found between groups ($p > 0.05$). These findings can be explained with basis on the surface energy values reported in Table 1, which show that pure HAp, pure XCA, XCA/XnHAp and XCA/XnHApSr have similar surface energy values. Therefore, the incorporation of Sr or XnHAp does not affect the surface energy values and, consequently, it has no substantial effect on osteoblast proliferation. This correlation is line with *in vitro* experiments, where incorporating Sr to HAp favored osteoblastic cell differentiation and mineralization, but it didn't stimulate the osteoblast proliferation [57].

On the other hand, the chemical composition of nanocomposites influenced ALP activity behavior. ALP is a cell membrane glycoprotein that catalyzes the hydrolysis of phosphate esters in alkaline pH, plays an important role in the mineralization process of bone matrix and its activity in human serum can be used as indicative for diseases related to liver and/or bone [58]. Fig. 7B shows the osteoblast ALP activity on day 21 determined for XCA, XCA/XnHAp and XCA/XnHApSr scaffolds. There was statistical difference in ALP activity between groups ($p < 0.05$). The ALP activity increased with the increase of filler content in both nanocomposites, but the increase was much more pronounced in the case of XCA/XnHApSr. In fact, the presence of strontium in the HAp structure (HApSr) seems to cause important effects in osteoblast and osteoclast growth. Literature reports showed that HApSr favors the increase of osteoblast ALP activity, the production of collagen type I and osteocalcin presence [14,57,59]. Ni and co-workers showed that upon enhancing the strontium incorporation in HAp, the stem cell differentiation into osteoblasts increased as well as the HAp solubility [57]. The HAp (CaP) mineral is very stable and has low solubility at physiological pH (7.2–7.6). The dissolution behavior of HAp is associated with osteogenic potential and osteoinductivity [60], which has been achieved with strontium inclusion, stimulating osteogenic behavior and bone formation [61].

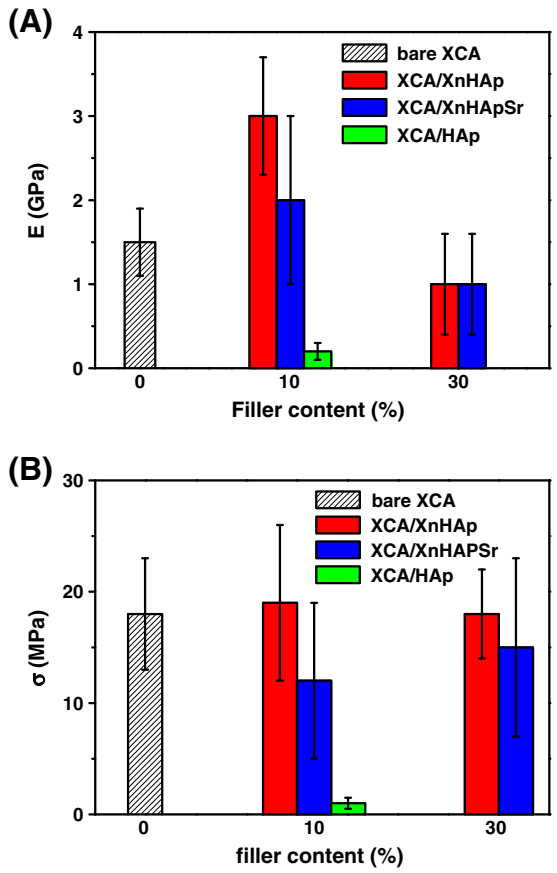

Fig. 5. (A) Young's modulus–E–and (B) stress at break–σ–measured for composites samples and bare XCA.

Table 1
Gel content and swelling ratio (Q) determined for hydrogels containing or not xanthan modified hydroxyapatite particles. Surface energy (γ^T) and the corresponding dispersive (γ^D) and polar (γ^P) components calculated for thin films of XCA, XCA/XnHAp 10% and XCA/XnHApSr 10% nanocomposite hydrogels.

Hydrogel sample	Gel content (%)	Q	γ^D mJ m^{-2}	γ^P mJ m^{-2}	γ^T mJ m^{-2}
XCA	77 ± 2	39 ± 6	30 ± 3	28 ± 3	58 ± 6
XCA/XnHAp 10%	78 ± 1	36 ± 7	30 ± 3	27 ± 3	57 ± 6
XCA/XnHApSr 10%	80 ± 3	40 ± 5	27 ± 3	31 ± 3	58 ± 6
HAp*	–	–	~33	~25	~58

* Data from dos Santos et al., 2008 [55].

4. Conclusions

Xanthan-hydroxyapatite (XnHAp) and its equivalent strontium substituted (XnHApSr) are easily obtained by precipitating hydroxyapatite in xanthan aqueous solution. Modifying hydroxyapatite particles with xanthan proved to be an advantageous strategy because it increases the particles surface charge density and, therefore, the colloidal stability. The enrichment of hydroxyapatite particles surfaces by xanthan chains (XnHAp or XnHApSr) enhanced not only the colloidal stability but also promoted the compatibility between crosslinked xanthan chains and XnHAp or XnHApSr particles. Nanocomposites made of crosslinked xanthan chains and 10 wt.% XnHAp were homogeneous and presented improved mechanical properties in comparison to bare xanthan networks or to nanocomposites with HAp. Nanocomposites presented porous structure, surface energy, gel content and swelling ratio comparable to bare xanthan hydrogels. Maybe this is the reason why cellular proliferation on xanthan hydrogels was not significantly increased by the inclusion of xanthan modified nanohydroxyapatites. On the other hand, the activity of ALP was substantially favored upon increasing XnHAp or XnHApSr content from 10% to 30%. Thus, the nanoparticle surface enrichment by xanthan chains plays an important role

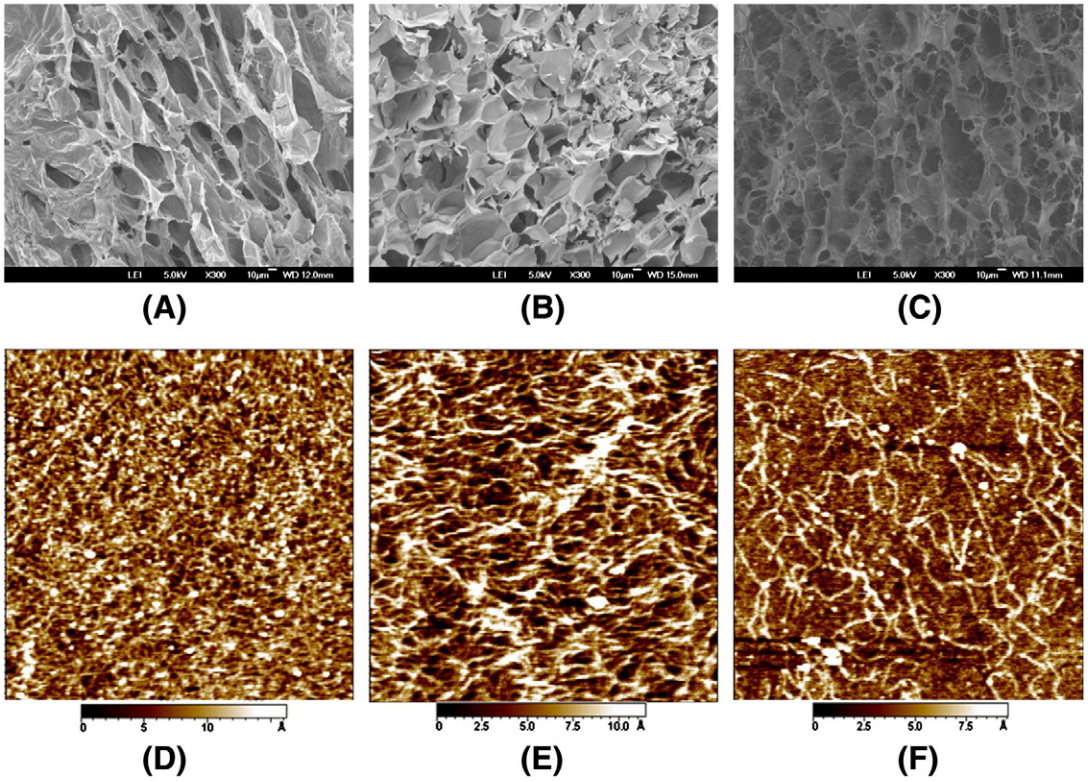

Fig. 6. SEM images from (A) XCA hydrogel, (B) XCA/XnHAp and (C) XCA/XnHApSr hydrogel composites. AFM images (scan area 2 μm × 2 μm) from (D) XCA, (E) XCA/XnHAp composite and (F) XCA/XnHApSr composite thin films.

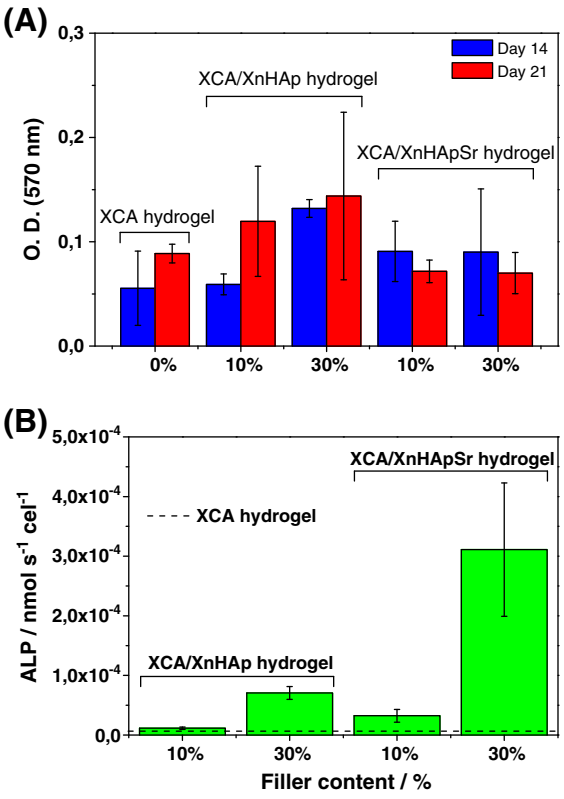

Fig. 7. Mean values with corresponding standard deviations determined for (A) osteoblast proliferation (normalized MTT activity) and (B) Alkaline phosphatase (ALP) activity at day 21.

to increase the compatibilization between hydroxyapatite and polysaccharide hydrogels, improving their biomedical application.

Acknowledgments

We thank the Brazilian Agency FAPESP (Grants 2010/13034-2, 2010/51219-5 and 2011/21442-6), Rede Nanobiotec CAPES and CNPq for the financial support.

Appendix A. Supplementary data

Supplementary data to this article can be found online at http://dx.doi.org/10.1016/j.msec.2014.01.002.

References

[1] H. Geckil, F. Xu, X. Zhang, S.J. Moon, U. Demirci, Engineering hydrogels as extracellular matrix mimics, Nanomedicine 5 (2010) 469–484.
[2] K.Y. Lee, D.J. Mooney, Hydrogels for tissue engineering, Chem. Rev. 101 (2001) 1869–1979.
[3] R. Barbucci, M. Consumi, S. Lamponi, G. Leone, Polysaccharides based hydrogels for biological applications, Macromol. Symp. 204 (2003) 37–58.
[4] M.R. Moura, F. Ahmad-Aouada, S.L. Favaro, E. Radovanovic, A.F. Rubira, E.C. Muniz, Release of BSA from porous matrices constituted of alginate-Ca^{2+} and PNIPAAm-interpenetrated networks, Mater. Sci. Eng. C 29 (2009) 2319–2325.
[5] R.A.A. Muzzarelli, C. Muzzarelli, Chitosan chemistry: relevance to the biomedical sciences, in: T. Heinze (Ed.), Polysaccharides I: Structure, Characterization and Use, Advances in Polymer Science, 186, 2005, pp. 151–209.
[6] L.N. Novikova, A. Mosahebi, M. Wiberg, G. Terenghi, J.-O. Kellerth, L.N. Novikov, Alginate hydrogel and matrigel as potential cell carriers for neurotransplantation, J. Biomed. Mater. Res. A 77A (2006) 242–252.
[7] N.C. Hunt, R.M. Shelton, L.M. Grover, An alginate hydrogel matrix for the localized delivery of a fibroblast/keratinocyte co-culture, Biotechnol. J. 4 (2009) 730–737.
[8] K.Y. Lee, L. Jeong, Y.O. Kang, S.J. Lee, W.H. Park, Engineering nanomedicines using stimuli-responsive biomaterials, Adv. Drug Deliv. Rev. 61 (2009) 1020–1030.
[9] S. Saska, R.M. Scarel-Caminaga, L.N. Teixeira, L.P. Franchi, R.A. Santos, A.M.M. Gaspar, P.T. Oliveira, A.L. Rosa, C.S. Takahashi, Y. Messaddeq, S.J.L. Ribeiro, R. Marchetto, Characterization and in vitro evaluation of bacterial cellulose membranes functionalized with osteogenic growth peptide for bone tissue engineering, J. Mater. Sci. Mater. Med. 23 (2012) 2253–2266.
[10] S. Saska, L.N. Teixeira, P.T. Oliveira, A.M.M. Gaspar, S.J.L. Ribeiro, Y. Messaddeq, R. Marchetto, Bacterial cellulose-collagen nanocomposite for bone tissue engineering, J. Mater. Chem. 22 (2012) 22102–22112.
[11] E.D. Eanes, Crystal growth of mineral phases in skeletal tissues, Prog. Cryst. Growth Charact. Mater. 3 (1980) 3–15.
[12] H. Zhou, J. Lee, Nanoscale hydroxyapatite particles for bone tissue engineering, Acta Biomater. 7 (2011) 2769–2781.
[13] P.J. Marie, Strontium as therapy for osteoporosis, Curr. Opin. Pharmacol. 5 (2005) 633–636.
[14] C. Capuccini, P. Torricelli, F. Sima, E. Boanini, C. Ristoscu, B. Bracci, G. Socol, M. Fini, I.N. Mihailescu, A. Bigi, Strontium-substituted hydroxyapatite coatings synthesized by pulsed-laser deposition: in vitro osteoblast and osteoclast response, Acta Biomater. 4 (2008) 1885–1893.
[15] G.X. Ni, K.Y. Chiu, W.W. Lu, Y. Wang, Y.G. Zhang, L.B. Hao, Z.Y. Li, W.M. Lam, S.B. Lu, K.D.K. Luk, Strontium-containing hydroxyapatite bioactive bone cement in revision hip arthroplasty, Biomaterials 27 (2006) 4348–4355.
[16] C.T. Wong, W.W. Lu, W.K. Chan, K.M.C. Cheung, K.D.K. Luk, D.S. Lu, A.B.M. Rabie, L.F. Deng, J.C.Y. Leong, *In vivo* cancellous bone remodeling on a strontium-containing hydroxyapatite (sr-HA) bioactive cement, J. Biomed. Mater. Res. A 68A (2004) 513–521.
[17] W. Suchanek, M. Yoshimura, Processing and properties of hydroxyapatite-based biomaterials for use as hard tissue replacement implants, J. Mater. Res. 13 (1998) 94–117.
[18] V. Nelea, C. Morosanu, M. Iliescu, I.N. Mihailescu, Microstructure and mechanical properties of hydroxyapatite thin films grown by RF magnetron sputtering, Surf. Coat. Technol. 173 (2003) 315–322.
[19] B. Viswanath, R. Raghavan, U. Ramamurty, N. Ravishankar, Mechanical properties and anisotropy in hydroxyapatite single crystals, Scr. Mater. 57 (2007) 361–364.
[20] M.L. Xu, X.S. Chen, A.X. Liu, Z.K. Hong, X.B. Jing, Electrospun poly(l-lactide)-grafted hydroxyapatite/poly(l-lactide) nanocomposite fibers, Eur. Polym. J. 43 (2007) 3187–3196.
[21] X.Y. Qiu, Z.K. Hong, J.L. Hu, L. Chen, X.S. Chen, X.B. Jing, Hydroxyapatite surface modified by L-lactic acid and its subsequent grafting polymerization of L-lactide, Biomacromolecules 6 (2005) 1193–1199.
[22] L. Lu, Q. YuSha, A. ChangRen, J. YanPeng, Rapidly in situ forming biodegradable hydrogels by combining alginate and hydroxyapatite nanocrystal, Sci. China E Technol. Sci. 53 (2010) 272–277.
[23] K. Madhumathi, K.T. Shalumon, V.V. Divya Rani, H. Tamura, T. Furuike, N. Selvamurugan, S.V. Nair, R. Jayakumar, Wet chemical synthesis of chitosan hydrogel-hydroxyapatite composite membranes for tissue engineering applications, Int. J. Biol. Macromol. 45 (2009) 12–15.
[24] S. Wang, S. Wen, M. Shen, R. Guo, X. Cao, J. Wang, X. Shi, Aminopropyltriethoxysilane-mediated surface functionalization of hydroxyapatite nanoparticles: synthesis, characterization, and in vitro toxicity assay, Int. J. Nanomedicine 6 (2011) 3449–3459.
[25] J. Li, D. Zhu, J. Yin, Y. Liu, F. Yao, K. Yao, Formation of nano-hydroxyapatite crystal in situ in chitosan–pectin polyelectrolyte complex network, Mater. Sci. Eng. C 30 (2010) 795–803.
[26] J. Zhang, Q. Wang, A. Wang, In situ generation of sodium alginate/hydroxyapatite nanocomposite beads as drug-controlled release matrices, Acta Biomater. 6 (2010) 445–454.
[27] L. Borum, O.C. Wilson, Surface modification of hydroxyapatite. Part II. Silica, Biomaterials 24 (2003) 3681–3688.
[28] O.C. Wilson Jr., J.R. Hull, Surface modification of nanophase hydroxyapatite with chitosan, Mater. Sci. Eng. C 28 (2008) 434–437.
[29] K. Haraguchi, Stimuli-responsive nanocomposite gels, Colloid Polym. Sci. 289 (2011) 455–473.
[30] K. Haraguchi, T. Takehisa, Nanocomposite hydrogels: a unique organic–inorganic network structure with extraordinary mechanical, optical, and swelling/deswelling properties, Adv. Mater. 14 (2002) 1120–1124.
[31] K. Kabiri, H. Omidian, M.J. Zohuriaan-Mehr, S. Doroudiani, Superabsorbent hydrogel composites and nanocomposites: a review, Polym. Compos. 32 (2011) 277–289.
[32] A. Dubnika, D. Loca, L. Berzina-Cimdina, Functionalized hydroxyapatite scaffolds coated with sodium alginate and chitosan for controlled drug delivery, Proc. Est. Acad. Sci. 61 (2012) 193–199.
[33] C. Chang, N. Peng, M. He, Y. Teramoto, Y. Nishio, L. Zhang, Fabrication and properties of chitin/hydroxyapatite hybrid hydrogels as scaffold nano-materials, Carbohydr. Polym. 91 (2013) 7–13.
[34] S. Laïb, B.H. Fellah, A. Fatimi, S. Quillard, C. Vinatier, O. Gauthier, P. Janvier, M. Petit, B. Bujoli, S. Bohic, P. Weiss, The in vivo degradation of a ruthenium labelled polysaccharide-based hydrogel for bone tissue engineering, Biomaterials 30 (2009) 1568–1577.
[35] R. Geremia, M. Rinaudo, Biosynthesis, structure, and physical properties of some bacterial polysaccharides, in: S. Dumitriu (Ed.), Polysaccharides: Structural Diversity and Functional Versatility, Marcel Dekker, New York, 2005.
[36] D.F.S. Petri, J.C. Queiroz-Neto, Identification of lift-off mechanism failure for salt drill-in drilling fluid containing polymer filter cake through adsorption/desorption studies, J. Pet. Sci. Eng. 70 (2010) 89–98.
[37] G. Han, G. Wang, X. Zhu, H. Shao, F. Lui, P. Yang, Y. Ying, F. Wang, P. Ling, Preparation of xanthan gum injection and its protective effect on articular cartilage in the development of osteoarthritis, Carbohydr. Polym. 87 (2012) 1837–1842.

[38] D. Bergmann, G. Furth, C. Mayer, Binding of bivalent cations by xanthan in aqueous solution, Int. J. Biol. Macromol. 43 (2008) 245–251.
[39] A.F. Dário, L.M.A. Hortêncio, M.R. Sierakowski, J.C. Queiroz Neto, D.F.S. Petri, The effect of calcium salts on the viscosity and adsorption behavior of xanthan, Carbohydr. Polym. 84 (2011) 669–676.
[40] V.B. Bueno, R. Bentini, L.H. Catalani, D.F.S. Petri, Synthesis and Swelling Behaviour of Xanthan-based Hydrogels, Carbohydr. Polym. 92 (2013) 1091–1099.
[41] V.B. Bueno, D.F.S. Petri, Xanthan hydrogels films: molecular conformation, charge density and protein carriers, Carbohydr. Polym. 101 (2014) 897–904.
[42] V.B. Bueno, A.M. Silva, L.R. Barbosa, L.H. Catalani, E. Teixeira-Neto, D.R. Cornejo, D.F.S. Petri, Hybrid composites of xanthan and magnetic nanoparticles for cellular uptake, Chem. Commun. 49 (2013) 9911–9913.
[43] M. Trécant-Viana, T. Le Neel, C. Canto-Nicolazo, E. Champion, M. Leroy, G. Daculsi, Dynamic Compaction of Biomaterial Powders, J. Phys. IV Proc. 7 (1997)(C3-3–C3-6).
[44] A.F. Dario, R.C.M. de Paula, H.C.B. Paula, J.P.A. Feitosa, D.F.S. Petri, Effect of solvent on the adsorption behavior and on the surface properties of Sterculia striata polysaccharide, Carbohydr. Polym. 81 (2010) 284–290.
[45] W.A. Adamson, Physical chemistry of surfaces, John Wiley & Sons, Toronto, 1990.
[46] A. Carré, V. Lacarrière, How Substrate Properties Control Cell Adhesion. A Physical–Chemical Approach, J. Adhes. Sci. Technol. 24 (2010) 815–830.
[47] D.K. Owens, R.C. Wendt, Estimation of the surface free energy of polymers, J. Appl. Polym. Sci. 13 (1969) 1741–1747.
[48] E.E. Golub, K. Boesze-Battaglia, The role of alkaline phosphatase in mineralization, Curr. Opin. Orthop. 18 (2007) 444–448.
[49] J.-K. Han, H.-Y. Song, F. Saito, B.-T. Lee, Synthesis of high purity nano-sized hydroxyapatite powder by microwave-hydrothermal method, Mater. Chem. Phys. 99 (2006) 235–239.
[50] S. Raynaud, E. Champion, D. Bernache-Assollant, P. Thomas, Calcium phosphate apatite with variable Ca/P atomic ratio I. Synthesis, characterisation and thermal stability of powders, Biomaterials 23 (2002) 1065–1072.
[51] M. Sadat-Shojai, Preparation of hydroxyapatite nanoparticles: comparison between hydrothermal and solvo-treatment processes and colloidal stability of produced nanoparticles in a dilute experimental dental adhesive, J. Iran. Chem. Soc. 6 (2009) 386–392.
[52] A. Bigi, E. Boanini, C. Capuccini, M. Gazzano, Strontium-substituted hydroxyapatite nanocrystals, Inorg. Chim. Acta 360 (2007) 1009–1016.
[53] R. Murugan, S. Ramakrishna, Production of ultra-fine bioresorbable carbonated hydroxyapatite, Acta Biomater. 2 (2006) 201–206.
[54] M.P. Ferraz, F.J. Monteiro, C.M. Manuel, Hydroxyapatite nanoparticles: a review of preparation methodologies, J. Appl. Biomater. Biomech. 2 (2004) 74–80.
[55] E.A. dos Santos, E.M. Farina, G.A. Soares, K. Anselme, Surface energy of hydroxyapatite and b-tricalcium phosphate ceramics driving serum adsorption and osteoblast adhesion, J. Mater. Sci. Mater. Med. 19 (2008) 2307–2316.
[56] K. Anselme, L. Ploux, A. Ponche, Cell/material interfaces: influence of surface chemistry and surface topography on cell adhesion, J. Adhes. Sci. Technol. 24 (2010) 831–852.
[57] G.X. Ni, Z.P. Yao, G.T. Huang, W.G. Liu, W.W. Lu, The effect of strontium incorporation in hydroxyapatite on osteoblasts in vitro, J. Mater. Sci. Mater. Med. 22 (2011) 961–967.
[58] J.E. Coleman, Structure and Mechanism of Alkaline Phosphatase, Annu. Rev. Biophys. Biomol. Struct. 21 (1992) 441–483.
[59] E. Boanini, P. Torricelli, M. Fini, A. Bigi, Osteopenic bone cell response to strontium-substituted hydroxyapatite, J. Mater. Sci. Mater. Med. 22 (2011) 2079–2088.
[60] H.P. Yuan, H. Fernandes, P. Habibovic, J. de Boer, A.M.C. Barradas, A. de Ruiter, W.R. Walsh, C.A. van Blitterswijk, J.D. de Bruijn, Osteoinductive ceramics as a synthetic alternative to autologous bone grafting, Proc. Natl. Acad. Sci. U. S. A. 107 (2010) 13614–13619.
[61] Y.C. Chai, A. Carlier, J. Bolander, S.J. Roberts, L. Geris, J. Schrooten, H. Van Oosterwyck, F.P. Luyten, Current views on calcium phosphate osteogenicity and the translation into effective bone regeneration strategies, Acta Biomater. 8 (2012) 3876–3887.